Phantom validation of Monte Carlo modeling for noncontact depth sensitive fluorescence measurements in an epithelial tissue model

Yi Hong Ong
Caigang Zhu
Quan Liu

Phantom validation of Monte Carlo modeling for noncontact depth sensitive fluorescence measurements in an epithelial tissue model

Yi Hong Ong,[†] Caigang Zhu,[†] and Quan Liu*
Nanyang Technological University, School of Chemical and Biomedical Engineering, Division of Bioengineering, Singapore 637457, Singapore

Abstract. Experimental investigation and optimization of various optical parameters in the design of depth sensitive optical measurements in layered tissues would require a huge amount of time and resources. A computational method to model light transport in layered tissues using Monte Carlo simulations has been developed for decades to reduce the cost incurred during this process. In this work, we employed the Monte Carlo method to investigate the depth sensitivity achieved by various illumination and detection configurations including both the traditional cone configurations and new cone shell configurations, which are implemented by convex or axicon lenses. Phantom experiments have been carried out to validate the Monte Carlo modeling of fluorescence in a two-layered turbid, epithelial tissue model. The measured fluorescence and depth sensitivity of different illumination–detection configurations were compared with each other. The results indicate excellent agreement between the experimental and simulation results in the trends of fluorescence intensity and depth sensitivity. The findings of this study and the development of the Monte Carlo method for noncontact setups provide useful insight and assistance in the planning and optimization of optical designs for depth sensitive fluorescence measurements. © *2014 Society of Photo-Optical Instrumentation Engineers (SPIE)* [DOI: 10.1117/1.JBO.19.8.085006]

1 Introduction

Fluorescence spectroscopy has been widely explored for the detection of precancers and cancers in human epithelial tissues.[1–3] Because it is an optical spectroscopic technique, fluorescence spectroscopy is capable of rapidly and noninvasively quantifying biochemical and morphological changes in human tissues due to the rich endogenous fluorophore contents in epithelial tissues that contain vital diagnostic information for the identification of tissue malignancy. Generally, an epithelial tissue consists of an outer epithelial layer that rests on the basement membrane and an underlying stromal layer. The distribution of these fluorophores in an epithelial tissue is depth dependent and can be affected by several factors, such as the age, menopausal status,[4,5] and disease progression.[6,7] The optical scattering property of epithelial tissues further complicates the *in-vivo* localization of these fluorophores. Thus, an optical setup of illumination and detection with excellent depth sensitivity is highly preferable to improve the diagnostic accuracy of this technique in epithelial precancer and cancer.

Depth sensitive fluorescence measurements have previously been demonstrated using contact fiber-optic-based probe geometries by varying the source-detector separation,[8] aperture diameter,[9] and tilt angle of illumination and collection fibers.[10] However, a fiber-optic-based probe requires contact with the sample surface and a past study has shown that the inconsistent pressure exerted on biological tissues can cause spectral distortion that severely affects the diagnostic accuracy of this technique.[11] Besides that, the contact between the probe and the patient's skin, especially on infectious sites, may cause probe contamination and elevates the risk of disease transmission across patients. To overcome these complications, alternative noncontact measurement methods have been investigated by using lens-based setups. Bish et al.[12] performed noncontact diffuse reflectance measurements on tissue phantoms and human skin by using a lens-based probe in an effort to eliminate the diagnostic inconsistency due to the exertion of probe pressure. Mazurenka et al.[13] demonstrated noncontact time-resolved diffuse reflectance measurements with a lens-based setup, and laser scanning was used to achieve the imaging. Generally, these lens-based setups use a combination of lenses to achieve the excitation and collection volumes that would form cones in an optically transparent medium. Even though the noncontact setup has the advantage of minimizing the risk of disease transmission and inconsistent probe-sample pressure exertion, it suffers from limited sensitivity to subsurface fluorescence signals due to the signal contribution from shallower layers in a layered structure, such as the epithelial tissue, which is similar to the noncontact fiber-optic-based setup.

Our group has previously demonstrated that a cone shell illumination configuration was able to improve the depth sensitivity of fluorescence signals from deep layers by reducing the contribution from the shallower layer. The term "depth sensitivity" in this study was defined as the ratio of the intensity of measured fluorescence originated from an individual layer to the total measured fluorescence. We have experimentally investigated the cone shell illumination configuration implemented by

*Address all correspondence to: Quan Liu, E-mail: quanliu@ntu.edu.sg

[†]These authors contributed equally.

multiple axicon lenses in a fluorescence study using a two-layered tissue phantom, which mimicked the optical properties of human skin.[14] The results showed that the cone shell illumination configuration was able to detect fluorescence signals with a higher sensitivity to the deep layer and a larger range of sensitivity to the top and bottom layers than a conventional cone configuration implemented by a convex lens. It has been demonstrated that the cone shell illumination configuration implemented by the axicon lenses exhibits enhanced depth sensitivity compared to the cone configuration implemented by a convex lens. Further, enhancement in depth sensitivity is expected through systematic optimization of various optical parameters, such as the diameter, height and apex angle of the axicon lens, lens-sample distance, the outer and inner diameters of the cone shell illumination beam, and so on. However, the experimental investigation of these parameters would require a huge amount of time and resources. For instance, an axicon lens with a fixed apex angle is needed to create a cone shell with a particular incident angle on the sample surface, but it is not cost effective to get multiple expensive axicon lenses with a full range of different apex angles for optimization.

To effectively reproduce the experimental configuration of these optical measurements without incurring significant cost, the Monte Carlo method has been developed and employed in the past few decades as a versatile computational tool to model light propagation in turbid tissue-like media. Optical configurations and light-tissue interactions (scattering, absorption, and fluorescence) can be modeled to simulate light distribution in the numerical model of human tissues, which has been extremely useful in helping the design and optimization of various experiments and optical setups. Keijzer et al.[15] used the Monte Carlo method to simulate fluorescence in turbid media and investigated the effect of the geometry in the excitation light delivery and emission light detection on measured signals. Wang and Jacque's versatile Monte Carlo simulation package[16,17] for the modeling of photon transport in multilayered tissues has been publicized and has received enormous attention. Welch et al.[18] have evaluated the effect of tissue optical properties and the geometry of a tissue sample using Monte Carlo simulations. In another Monte Carlo simulation study, Qu et al.[19] demonstrated that maximizing the overlap between the illumination and detection area can reduce the distortion in measured fluorescence signals due to variation in the tissue optical property with wavelength. In achieving depth sensitive fluorescence measurement, Zhu et al.[20] used Monte Carlo simulations to model different contact fiber-optic based probe geometries in fluorescence measurements from different depths in epithelial tissues. Recently, Zhu and Liu[21] from the authors' group have simulated the cone and cone shell configuration implemented by a convex lens in a noncontact imaging geometry using the Monte Carlo method, and the results showed that the cone shell configuration yields a larger sensitivity to fluorescence from deep layers.

Although the Monte Carlo method has been widely employed to study light propagation in turbid media, limited works on the experimental validation of the Monte Carlo modeling have been reported. Pogue et al.[22] used the Monte Carlo method to study the fluorescence measured from tissue samples using a fiber bundle with an individual fiber diameter of 100 μm, in which experiments were performed to verify the results. Liu and Ramanujam[10] used Monte Carlo modeling to simulate fluorescence measured from turbid tissue phantoms

by an angled fiber-optic probe, and demonstrated that depth selectivity can be achieved by varying the illumination angles. The simulation results have been verified with experiments using two-layered epithelial tissue phantoms. Liu et al.[23] have also used the Monte Carlo method to simulate fluorescence and diffuse reflectance values measured by several different fiber-optic probe geometries that were designed to sample small tissue volumes. They quantitatively compared the numerically simulated and experimentally measured results to validate the Monte Carlo model.

Even though there has been an increasing interest in using the Monte Carlo method to simulate fluorescence light transport in turbid media, most previous reports focused on using fiber-optic-based probe geometries for illumination and detection. Investigation on noncontact lens-based probe geometries using the Monte Carlo method has been very limited. The goal of this study is to experimentally verify the Monte Carlo modeling of fluorescence measurements involving noncontact lens-based probe geometries from turbid media with a layered structure. We have developed a Monte Carlo model to simulate different combinations of illumination and detection configurations, involving both the cone and cone shell geometry, on a tissue model. In particular, simulations and experiments were carried out to assess the depth sensitivity performance of different combinations of illumination and detection configurations in a noncontact lens-based probe geometry, implemented by axicon or convex lenses, in a two-layered turbid medium mimicking the optical properties of human epithelial tissues.

In our previous work,[14] we have compared the depth sensitivity achieved by a cone (illumination)-cone (detection) configuration implemented by a convex lens and a cone shell (illumination)-cone (detection) configuration an axicon lens. In this work, we further expand our previous investigation by including more illumination and detection configurations, both numerically and experimentally. The simulation results are validated with the experimental results in terms of fluorescence intensities at the emission peaks and the depth sensitivity to a given layer. The experimental results provide useful insights to the change in depth sensitivity achieved using different types of lenses and illumination-detection geometries. The development and validation of this Monte Carlo code provide a fast, inexpensive, reliable, and robust computational platform that can assist the planning and optimization of optical designs involving the cone or cone shell illumination and detection geometries prior to the physical development of an optical system for real experiments.

2 Experimental Setups

In this study, we investigated four different illumination and detection configurations involving both the cone and cone shell geometries. The four illumination-detection configurations are shown in Fig. 1, where (a) represents a cone (illumination)-cone (detection) and (b) a cone shell-cone configuration implemented by a convex lens, (c) a cone shell-cone configuration, and (d) a cone shell-cone shell configuration implemented by an axicon lens.

The noncontact probe for configurations (a) and (b) in Fig. 1 was coupled to a diode laser (iFlex-2000, Point Source Ltd., Hamble, UK) with a maximum output power of 50 mW at 405 nm, as shown in Fig. 2(a). The output laser light with a beam diameter of around 1 mm was expanded using a 30x beam expander before passing through a 405 nm bandpass filter
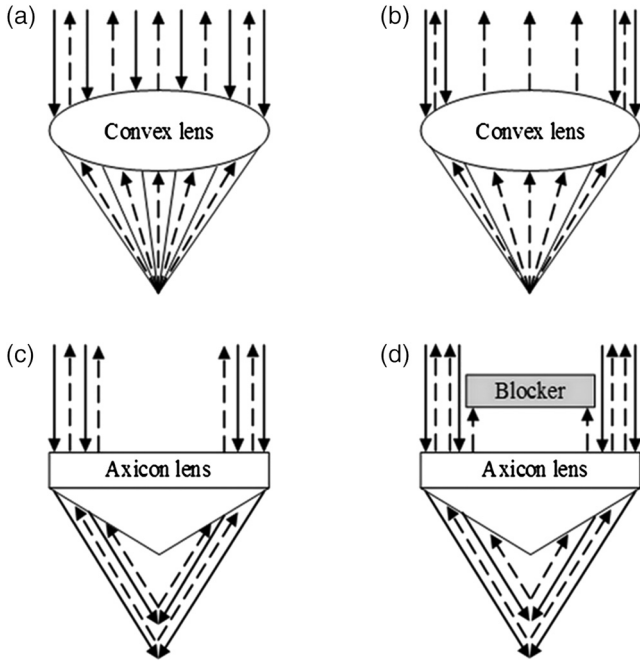
(a)

Convex lens

(b)

Convex lens

(c)

Axicon lens

(d)

Blocker

Axicon lens

Fig. 1 Schematic diagram of four illumination-detection configurations: (a) cone-cone, (b) cone shell-cone, (c) cone shell-cone and (d) cone shell-cone shell. Configurations (a) and (b) are implemented using convex lens; configurations (c) and (d) are implemented using axicon lens. The solid arrow represents the excitation laser light while the dashed arrow represents the emitted fluorescence light.

and was then deflected by a dichroic mirror toward a convex lens ($f = 35$ mm) with a diameter of 25.4 mm, in which the lens was slightly overfilled. A piece of aluminum sheet with a diameter of 23.4 mm was placed along the excitation light path between the beam expander and bandpass filter, to create a cone shell illumination configuration as shown in Fig. 1(b). The fluorescence signal was collected through the same convex lens, which passed through the dichroic mirror and a longpass filter before being focused onto the core of a collection fiber, with a diameter of 400 μm and numerical aperture (NA) of 0.22, by a convex lens ($f = 35$ mm).

The noncontact probe for configurations (c) and (d) in Fig. 1 was constructed as shown in Fig. 2(b). For the configuration in Fig. 1(c), a collimated beam of around 3 mm in diameter was passed through a pair of axicon lenses with an apex angle of 140 deg to form an annular laser beam. The excitation beam was passed through a bandpass filter and deflected by a dichroic mirror toward a third axicon lens with an apex angle of 110 deg,

which formed a cone shell illumination configuration. The fluorescence signal was collected by the third axicon lens and focused onto the collection fiber as described above. The configuration in Fig. 1(d) was the same as the configuration in Fig. 1(c), except that a piece of circular aluminum sheet was placed on the third axicon lens to block the fluorescence signal that came back through the center of the lens to create a cone shell detection configuration. The collected fluorescence signal was transmitted by the collection fiber to a Czerny-Turner type spectrograph (Shamrock 303, Andor Technology, Belfast, UK) and a research-grade charge coupled device (DU920P-BR-DD, Andor Technology, Belfast, UK). The laser powers measured on the sample surface were around 2.5 mW for configurations (a) and (b), and 7 mW for configurations (c) and (d). The integration time for each measurement was 1 s in all experiments.

During measurements, the phantom was placed on a translational stage underneath the probe. For configurations (a) and (b), the probe-sample distance was varied to measure from different depths in the phantom by raising the stage toward the probe. The first measurement started at 0 mm where the focal spot of the excitation light was located on the surface of the phantom. Then, for every subsequent measurement, the stage was raised by 0.5 mm until it reached a depth of 4 mm beneath the surface. The integration time for each spectrum was 1 s and the laser shutter was closed for 10 s between each measurement to allow fluorescence recovery in case of the possible photobleaching of fluorophores.

For configurations in Figs. 1(c) and 1(d), three plano-convex axicon lenses were used to map the axial dimension (depth) to the radial dimension (radius). An axicon lens can steer a collimated light at a fixed angle relative to the conical surface. Thus, by varying the radius of a collimated illumination light ring, it can focus the light at various depths thereby, eliminating the need to move the probe up or down for depth sensitive measurements. In our setup, a plano-convex axicon lens (Axicon 3 in Fig. 3), with an apex angle (α_2) of 35 deg was used for illumination and detection. The relationship between α and β as labeled in Fig. 3 is given as

$$\beta_N = \sin^{-1}(n \sin \alpha_N) - \alpha_N, \qquad (1)$$

where n is the refractive index of the material of which the axicon lens is made and N is the index of the angle.

All axicon lenses were made up of BK7 glass with a refractive index of 1.51 at 785 nm, and the β_2 was calculated to be 25 deg. By using the Pythagoras theorem, the maximum depth of focus from the apex of Axicon 3 (L_2) can be calculated as shown below:
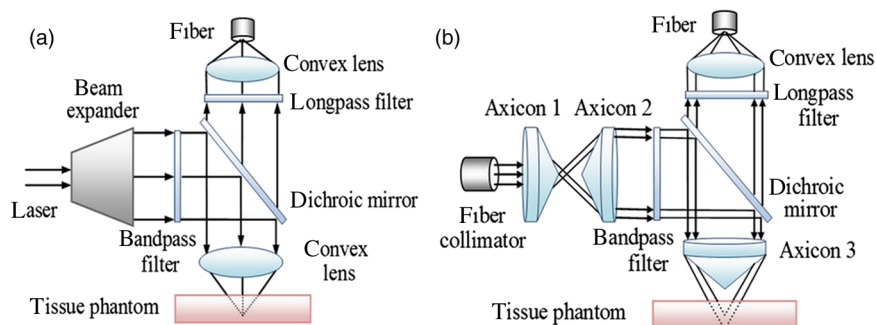
(a)

Fiber

Convex lens

Beam expander

Longpass filter

Laser

Dichroic mirror

Bandpass filter

Convex lens

Tissue phantom

(b)

Fiber

Convex lens

Axicon 1 Axicon 2

Longpass filter

Fiber collimator

Dichroic mirror

Bandpass filter

Axicon 3

Tissue phantom

Fig. 2 Schematic diagram of the system setup based on the combination of (a) convex lenses and (b) axicon lenses. [Adapted from Ong and Liu [14] with permission].
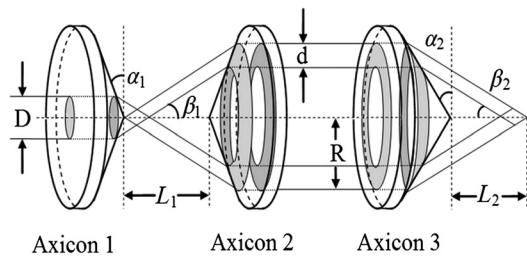
Fig. 3 Schematic diagram of the axicon lens-based setup. Axicons 1 and 2 are used to create collimated laser ring; Axicon 3 is used to create light with the cone shell geometry.

$$L_2 = R \left(\frac{1}{\tan \beta_2} - \tan \alpha_2 \right), \tag{2}$$

where R is the outer radius of the illumination light after axicon lens 2.

Equation (2) indicates that the depth of focus, L_2, changes with the outer radius of the illumination light, R. In order for Axicon 3 to form a cone shell illumination configuration, a collimated laser ring is needed. The excitation laser ring can be created by passing a collimated laser through a pair of identical plano-convex axicon lenses ($\alpha_1 = 20$ deg) with apexes facing each other, as shown in Figs. 2(b) and 3. The diameter of the laser ring can be manipulated by changing the distance between the plano-convex axicon pair. The relation between the distance, L_1, and the ring radius, R, can be deduced by using Eq. (3)

$$R = \frac{L_1}{\left(\frac{1}{\tan \beta_1} - \tan \alpha_1 \right)}. \tag{3}$$

Therefore, the depth of laser focus, without changing the distance between the axicon lens' tip and the sample surface, varies with the outer radius of the beam R, which can be changed by varying the distance between Axicons 1 and 2 as shown in Table 1.

As the diameter of the excitation laser beam, D, incident on Axicon 1 was 3 mm, the smallest outer ring radius that can be created by Axicon 2 was 1.5 mm, which corresponds to a

Table 1 Relationship between the separation distance between axicon lens 1 and axicon lens 2, L_1 (mm), the outer radius, R (mm), of the collimated excitation annular ring, the maximum depth of focus for the apex of axicon lens 3, L_2 (mm) and the apparent depth of focus (mm) on tissue phantom.

L_1 (mm)	R (mm)	L_2 (mm)	Apparent depth of focus (mm)
7.1	1.5	2.17	0
9.5	2.0	2.89	0.72
11.8	2.5	3.61	1.44
14.2	3.0	4.33	2.16
16.6	3.5	5.06	2.89
18.9	4.0	5.78	3.61
20.4	4.3	6.17	4.00

minimum focal depth of 2.17 mm away from the apex of Axicon 3, as shown in Table 1. Therefore, in the experimental setup, the phantom was placed at a distance 2.17 mm below the probe tip (apex of Axicon 3), so that the focal spot of the laser is exactly located on the surface of the sample when the distance between Axicons 1 and 2 was 7.1 mm. Similarly, other apparent focal depth values were achieved according to Table 1. The apparent depth of focus refers to the targeted depth in an optically transparent medium. The probe–sample distance was fixed at 2.17 mm and remained unchanged throughout the experiments. Measurements were taken for an apparent focal depth range of 4 mm with an increment of 0.5 mm in order to be consistent with the measurements of configurations (a) and (b).

3 Sample Preparation

A two-layered agar phantom was prepared according to the recipe and procedure published in an earlier report.[24] The optical properties of the phantom were chosen to represent human cervical tissue.[25] The phantom was made in a cylindrical plastic petri dish with a diameter of 30 mm, in which the top layer was 500 μm while the bottom layer 10 mm to represent a semi-infinite medium. Two different fluorophores, flavin adenine dinucleotide (FAD) with a peak emission at 530 nm and protoporphyrin IX (PpIX) with a peak emission at 630 nm, were added into the top and bottom layers, respectively, for the ease of fluorescence discrimination from each layer. The concentration of FAD was 33.2 μM and the concentration of PpIX was 32.3 μM. Polystyrene spheres (07310, Polysciences, Warrington, Pennsylvania, USA) and nigrosin (N4754, Sigma-Aldrich, St. Louis, Missouri, USA) served as the light scatterers and absorbers. The concentration of polystyrene spheres needed to mimic the scattering coefficient of tissue at 530 nm was estimated using Mie theory and the concentration of nigrosin used to mimic the absorption coefficient of the tissue was calculated according to the measured extinction coefficient spectrum. The typical absorption and scattering coefficient spectra of epithelial tissue are different from those of the elastic scatterers (polystyrene spheres) and light absorbers (nigrosin) in shape from the excitation wavelength (405 nm) to the emission peak wavelengths (530 and 630 nm). Thus, the optical properties of the tissue phantom were chosen to match those of the epithelial tissue at the central wavelength, around 530 nm, in order to simulate and investigate depth sensitive fluorescence measurements as close to the real epithelial tissue as possible. A piece of plastic wrap was placed between the top and bottom layers to prevent the diffusion of phantom contents across the two layers. The thickness of the plastic wrap was measured to be 10 μm and no fluorescence signal from the plastic wrap was observed in the experiment.

The optical properties of the top and bottom layers of the tissue phantom at the excitation and emission wavelengths were listed in Table 2.

4 Monte Carlo Modeling

The Monte Carlo method for simulating convex lens-based light illumination and detection has been previously described in detail.[21] The simulation of fluorescence is based on a method proposed by Liu et al earlier.[23] The Monte Carlo method for the simulation of axicon lens-based light illumination and detection has never been reported before, and the details are described as follows.

Table 2 Optical properties (μ_s [cm^{-1}] and μ_a [cm^{-1}]) for top and bottom layers for tissue phantom at the excitation wavelength and at the peak emission wavelength of FAD and PpIX.

	Wavelength (nm)		
Layer	405 (Excitation)	530 (FAD)	630 (PpIX)
Top	39.7, 1.2	34.2, 1.9	26.2, 1.8
Bottom	250.2, 1.4	215.1, 2.2	185.7, 2.1

The schematic of axicon lens-based light illumination and detection is shown in Fig. 4. In the illumination module of the code, the radius of the axicon lens, the ring thickness, the apex angle, the thickness, and the distance between the axicon lens and tissue surface can be specified according to the experimental configuration. These five parameters are denoted by R, d, α, d_0, and d_1, respectively, in Fig. 4. The key step to be simulated for each launched photon is to find the incident location and the incident angle. The incident location of the photon on the surface of the tissue model can be determined in two steps. The first step is to find the incident location of the photon on the plano surface of the axicon lens. For the collimated beam created by a fiber followed by a beam collimator, which is the case in this study, the spatial distribution of photons can be assumed to be Gaussian. Therefore, the radial position of a photon on the axicon lens surface can be sampled by

$$r = \sqrt{R^2 - d^2 * \varepsilon_r}, \qquad (4)$$

where ε_r is a random number between 0 and 1 following a Gaussian distribution. The azimuthal angle of the photon was sampled by

$$\theta = 2\pi\varepsilon_\theta, \qquad (5)$$

where ε_θ is a random number uniformly distributed between 0 and 1. The Cartesian coordinates of the incident location on the top surface of the axicon lens in Fig. 4(a) are

$$x_{\text{lens}} = r * \cos\theta, \qquad (6)$$

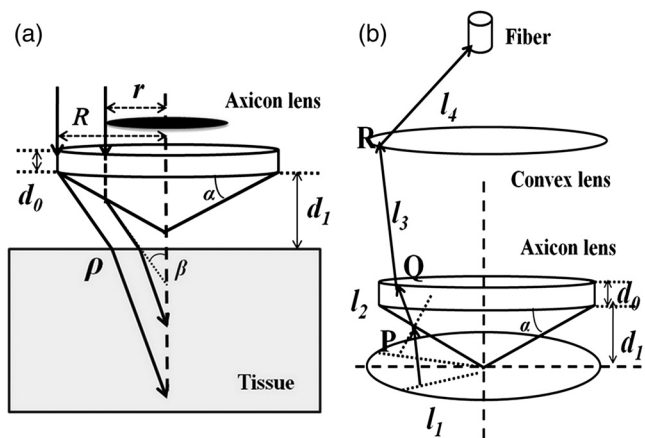$$y_{\text{lens}} = r * \sin\theta. \qquad (7)$$

Fig. 4 Schematic of axicon lens based (a) light illumination, (b) light detection.

Then, in the second step, the incident location on the tissue surface can be easily obtained by applying Snell's law based on x_{lens}, y_{lens}, d_1 and β that can be calculated from α. Once the photon moved onto the tissue surface, Snell's law is applied to calculate the incident angle at the air-tissue interface due to the mismatch of refractive index between the air and tissue models. Based on the incident deflection angle and the incident location on the tissue surface, it would be straightforward to find the directional cosine.

In the detection module as shown in Fig. 4(b), the parameters to be specified include the distance between the axicon and the convex lenses used for focusing light onto the detection fiber, the radius and focal length of the convex lens, and the size and NA of the detection fiber. The detection fiber, and the convex and the axicon lenses share the same common central axis passing through the origin of the Cartesian system. The tip of the detection fiber is located on the focal plane of the convex lens. The ray tracing procedure for a photon exiting from the tissue surface can be divided into seven steps described as follows:

Step 1: find the intersection P between the exit path of the photon l_1 and the tapered surface of the axicon lens;

Step 2: determine the directional vector of photon refraction on the tapered surface of the axicon lens labeled as l_2 by Snell's law;

Step 3: find the intersection Q between l_2 and the top surface of the axicon lens;

Step 4: determine the directional vector (l_3) of photon refraction on the top surface of the axicon lens by Snell's law;

Step 5: find the intersection R between l_3 and the convex lens;

Step 6: determine the directional vector (l_4) of photon refraction through the convex lens;

Step 7: determine whether l_4 fulfills the conditions for the exit photon to be detected by the fiber.

The values of all simulated parameters were equal to those in our experimental study. A total of 0.5×10^6 photons were used in each simulation and every simulation was repeated three times to calculate the standard deviation.

5 Data Analysis

Background subtraction was performed on all measured spectra. The background spectrum was acquired for every set of experiment with the excitation laser source switched off. The peak intensities at 530 and 630 nm were used for the plotting of FAD and PpIX fluorescence signal changes over a range of targeted depths in each configuration. The FAD peak intensity measured at every depth was divided by the maximum among these intensities to achieve the normalization. Similarly, the PpIX peak intensity measured at every depth was divided by the maximum among these intensities to obtain the normalized PpIX intensity. This method of normalization facilitated the comparison of the experimental results across different experimental setups by cancelling out the effect of different excitation laser powers on the sample due to the variation in optical setups. To compare the depth sensitivity achieved by each configuration, the sensitivities of the measured fluorescence to the top and bottom layers as a function of the targeted depth were computed. The sensitivity to the top or bottom layers at a particular

depth was computed by dividing the normalized FAD or PpIX intensities at this depth to the sum of the normalized FAD and PpIX intensities at the same depth.

In Monte Carlo simulations, the quantum yield of the fluorophore was always set to 1 and a combined absorption coefficient was used to account for two distinct absorption coefficients of the absorber and fluorophores. To compare the experimental and simulated results, the quantum yields of FAD and PpIX at both emission wavelengths had to be rescaled to the measured values and the absorption coefficients contributed separately by the absorber (nigrosin) and fluorophores (FAD and PpIX) in the tissue phantom had to be accounted for in the Monte Carlo simulations. In Monte Carlo simulations, the absorption coefficient of the phantom model indicates the probability of an excitation photon being absorbed by nigrosin or FAD/PpIX molecules, while the quantum yield of a fluorophore indicates the probability that an absorbed photon was converted into fluorescence light. The conversion of the absorption coefficient and rescaling of quantum yields from the experimentally measured values to the assigned value in simulations have been discussed in detail in the previous publication.[23] The absorption coefficients of nigrosin, FAD, and PpIX at the excitation wavelength were experimentally measured using a UV-VIS spectrophotometer (UV-2450, Shimadzu Corp., Kyoto, Japan) at the individual concentrations used in the tissue phantom, respectively. For a photon being absorbed or scattered according to the random sampling in the top layer, its probability of being absorbed by FAD molecules was calculated by taking the ratio of the absorption coefficient of FAD to the sum of absorption coefficients of nigrosin and FAD. Similarly, for a photon being absorbed or scattered according to the random sampling in the bottom layer, the probability of excitation light being absorbed by PpIX was calculated by taking the ratio of absorption coefficient of PpIX to the sum of absorption coefficients of nigrosin and PpIX.

To determine the quantum yield of FAD and PpIX in the tissue phantom for the purpose of the simulation, the fluorescence spectra of FAD and PpIX were measured at very low concentrations first to minimize the secondary absorption effect of the fluorophore itself on emitted fluorescence. Background subtraction was performed on the spectra, and then their intensities were scaled up to the fluorophores' concentrations used in the tissue phantom given that the fluorescence intensity is linearly proportional to the concentration of the fluorescence molecule in the concentration range in this study. The quantum yield of FAD at 530 nm was determined by taking the ratio of the FAD fluorescence intensity to the sum of FAD and PpIX fluorescence intensities at 530 nm. The quantum yield of PpIX at 530 nm was computed by taking the ratio of the PpIX fluorescence intensity to the sum of FAD and PpIX fluorescence intensities at 530 nm. The quantum yields of FAD and PpIX at 630 nm were similarly determined.

The simulated results, after the correction for both the absorption coefficient and quantum yield, were normalized in the same manner as in the processing of experimental data as described earlier to facilitate the comparison of FAD and PpIX fluorescence trends between the computational and experimental results. Then, the sensitivities to the top and bottom layers of each simulated configuration were computed using the same method as described above to further validate the Monte Carlo modeling that we have developed.

6 Results and Discussions

Figure 5 shows the trends of measured FAD and PpIX fluorescence and the sensitivities to the top and bottom layers in the cone-cone configuration for which the schematic is shown in Fig. 1(a). The experimental results are represented by solid lines and the simulation results are represented by dotted lines. The experiments were repeated three times at different locations on the same phantom, and the lens-sample distance was precisely adjusted using a translational stage. The standard deviations in the experimental results are small and are not shown on the plot as they cannot be seen clearly at most points. In Fig. 5(a), it is seen that the measured FAD fluorescence rises slightly at the beginning and reaches its maximum at around 0.7 mm before decreasing gradually to around 0.22 at a focal depth of 5.5 mm. In Fig. 5(b), the measured PpIX fluorescence reaches a maximum at around 0.7 mm and then decreases slowly to 0.38 at a focal depth of 5.5 mm. The simulated fluorescence of FAD and PpIX is also the highest at around 0.7 mm and decreases to around 0.2 and 0.3, respectively, at a focal depth of 5.5 mm. The overall trends in the simulated results are very similar to those of the measured results. The slight mismatch between the experimental and simulated results observed at focal depths of 3 mm or longer could potentially be attributed to a few factors that were not well controlled. For example, water evaporation from the tissue phantom during sample preparation or measurement could cause changes in the optical properties and fluorophore concentrations of the phantom.

Figures 5(c) and 5(d) show the experimental and computational sensitivities to the top and bottom layers for the cone-cone configuration. The experimental sensitivity to the top layer is 0.49 at zero focal depth and reaches its peak of 0.5 at a focal depth of 0.7 before decreasing to 0.38 at a focal depth of 5.5 mm, while the experimental sensitivity to the bottom layer reaches the lowest value of 0.5 at a focal depth of 0.7 mm and increases to 0.62 at a focal depth of 5.5 mm. The simulated sensitivity to the top layer is the highest value of 0.51 at zero focal depth and decreases continuously to 0.39 at a focal depth of 5.5 mm, while the simulation sensitivity to the bottom layer is the lowest value of 0.49 at zero focal depth and rises to the maximum of 0.61 at a focal depth of 5.5 mm. The overall trends of the sensitivities to the top and bottom layers in the experimental and simulated results agree with each other except at the first measurement point for the zero focal depth. This difference is probably due to the uncertainty in the localization of zero focal depth in the experiment. As the position of zero focal depth in the experiment was visually determined by searching for the smallest laser spot on the phantom surface, it might be slightly different from the actual position corresponding to zero focal depth that can be set precisely in the Monte Carlo simulations.

Figure 6 shows the trends of measured FAD and PpIX fluorescence and the sensitivities to the top and bottom layers in the cone shell-cone configuration implemented by a convex lens. In Fig. 6(a), it is seen that the measured FAD fluorescence rises from 0.88 at zero focal depth and reaches its maximum at around 0.7 mm before decreasing gradually to around 0.11 at a focal depth of 5.5 mm. It should be noted that FAD fluorescence in this configuration decreases faster after the maximum at a focal depth of 0.7 mm than that in the cone-cone configuration as shown in Fig. 5(a). This shows that the cone shell illumination geometry can be used to reduce the fluorescence contribution from shallower layers when performing deep measurements
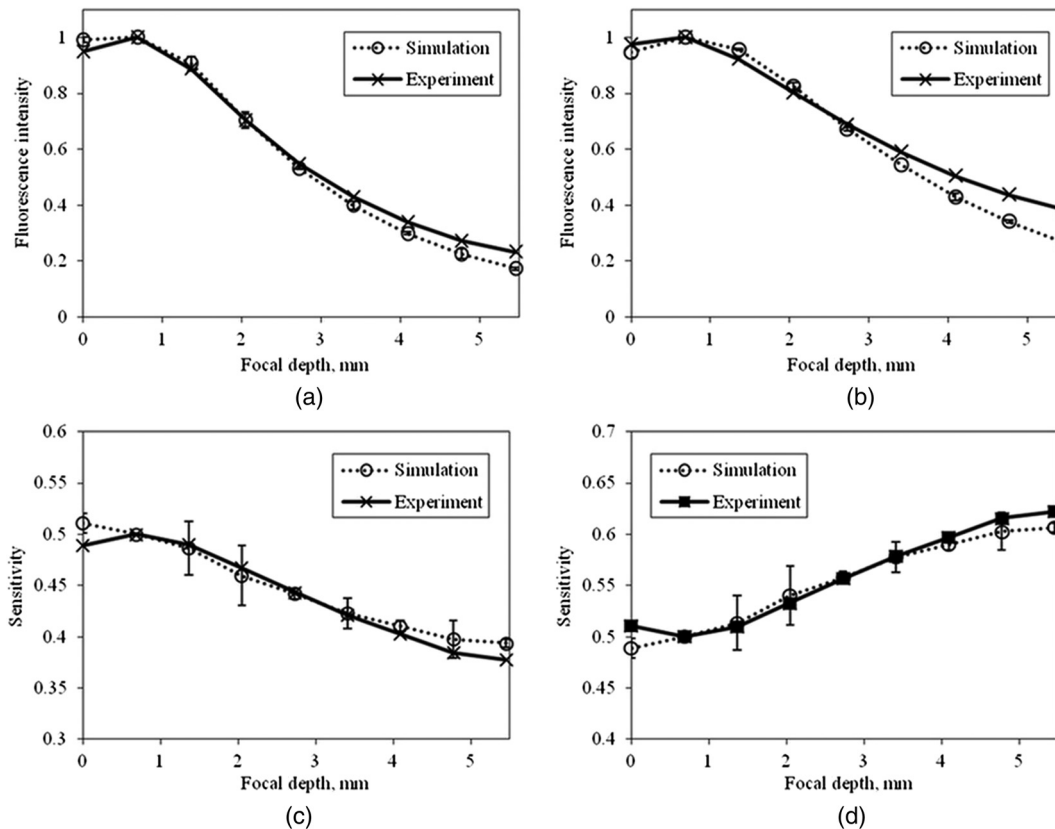
Fig. 5 (a) Normalized FAD fluorescence and (b) normalized PpIX fluorescence measured from the tissue phantom using the cone-cone configuration as shown in Fig. 1(a), and the corresponding Monte Carlo simulation results, (c) sensitivity to top layer and (d) sensitivity to bottom layer computed from the experimental and simulated results. Focal depth refers to the targeted depth of focus beneath the phantom surface, which has been corrected for the refractive mismatch between the phantom and air.

in a turbid medium, which agrees well with our previous report.[14] In Fig. 6(b), the measured PpIX fluorescence rises from 0.94 at the zero focal depth to its maximum at a focal depth of 0.7 mm, and then decreases slowly to 0.25 at a focal depth of 5.5 mm. The simulated FAD and PpIX fluorescence trends are in excellent agreement.

The experimental and simulated sensitivities to the top and bottom layers for the cone shell-cone configuration are shown in Figs. 6(c) and 6(d). Both experimental and simulated results show sensitivity to the top layer of 0.48 at the zero focal depth and 0.5 at a focal depth of 0.7 mm. Then, the experimental sensitivity to the top layer falls to 0.3 at a focal depth of 5.5 mm, while the simulated sensitivity drops to 0.28 at the same focal depth. The sensitivity to the bottom layer in both experimental and simulated results is 0.52 at a zero focal depth and drops to 0.5 at a focal depth of 0.7 mm before increasing to 0.70 and 0.72 at a focal depth of 5.5 mm, respectively. The trends in which the sensitivities to the top and bottom layers shift upon an increase in focal depth for both the experimental and simulated results agree with each other and the relatively larger range of sensitivities achieved as shown in Figs. 6(c) and 6(d) compared to Figs. 5(c) and 5(d) suggest that the cone shell illumination configuration is able to reduce the fluorescence from the overlaying layers in a turbid medium during deep measurements, hence improving the contrast of the targeted subsurface fluorescence.

Figure 7 shows the trends of measured FAD and PpIX fluorescence and the sensitivities to the top and bottom layers in the

cone shell-cone configuration as illustrated in Fig 1(c). The lens-sample distance was fixed throughout the measurements and the focal depth was varied by adjusting the distance between Axicons 1 and 2. Both of the axicon lenses were mounted in a cage system, where the position of Axicon 1 was fixed and Axicon 2 can be slid toward or away from Axicon 1 then secured. The positions of Axicon 2 in the cage to achieve the nine focal depths were marked on the cage rods in order to reduce the experimental variation in repeated measurements. The standard deviations in the experimental results are slightly higher than those in the convex lens-based setup as indicated by the error bars in Fig. 6. In Fig. 7(a), it is seen that the measured FAD fluorescence rises from the zero focal depth and reaches the maximum at around 0.7 mm. After that, the measured FAD fluorescence decreases to around 0.2 at a focal depth of 5.5 mm. In Fig. 7(b), the measured PpIX fluorescence rises from a zero focal depth and reaches the maximum at around 1.3 mm. Then, the measured PpIX decreases slowly to 0.37 at a focal depth of 5.5 mm. The trends in the simulated results are similar to the measured results.

Figures 7(c) and 7(d) show the sensitivities of the cone shell-cone configuration to the top and bottom layers, respectively. The sensitivity to the top layer in both experiment and simulation are around 0.54 at a zero focal depth. The sensitivity value drops as the focus moves toward the bottom layer and reaches around 0.31 in the experimental result and 0.29 in the simulated result at a focal depth of 5.5 mm. The sensitivities to the bottom layer in both sets of results are around 0.46 at the zero focal
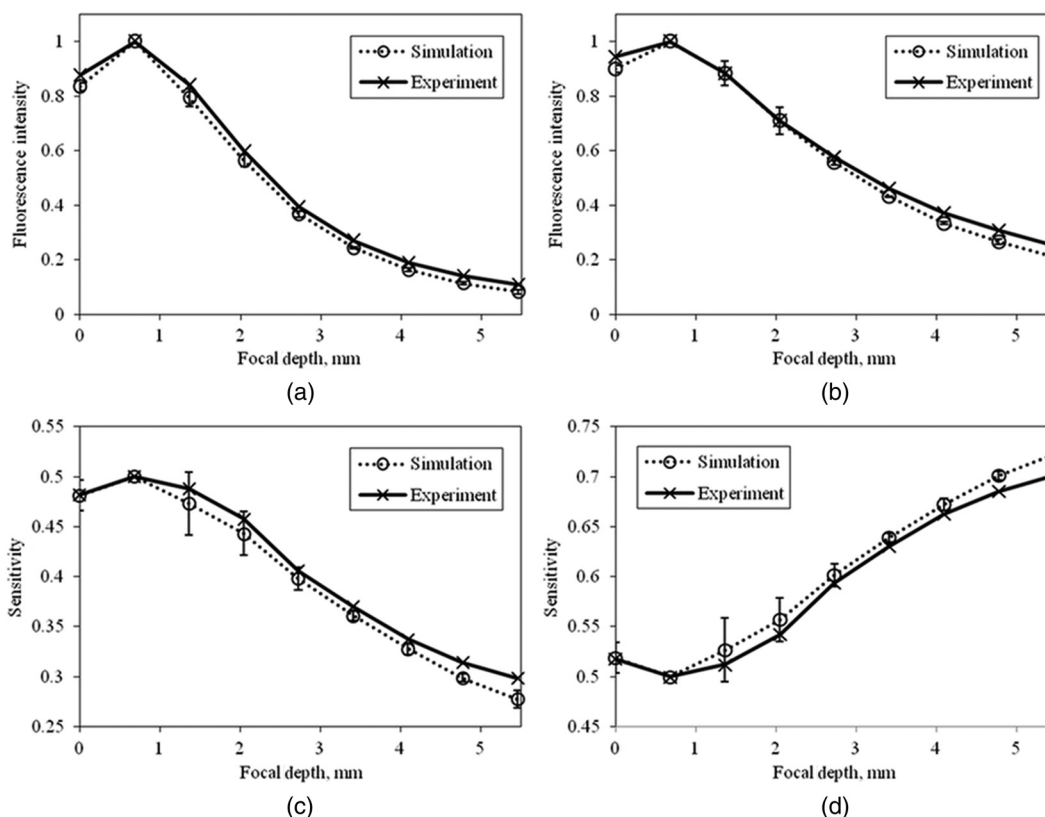
Fig. 6 (a) Normalized FAD fluorescence and (b) normalized PpIX measured from the tissue phantom using the cone shell-cone configuration as shown in Fig. 1(b), and the corresponding Monte Carlo simulation results, (c) sensitivity to top layer and (d) sensitivity to bottom layer computed from the experimental and simulated results. Focal depth refers to the targeted depth of focus beneath the phantom surface, which has been corrected for the refractive mismatch between the phantom and air.

depth and increase to around 0.69 in the experimental result and 0.71 in the simulated result at a focal depth of 5.5 mm.

Figure 8 shows the trends of measured FAD and PpIX fluorescence intensities and the sensitivities to the top and bottom layers for the cone shell-cone shell configuration as illustrated in Fig. 1(d). In Fig. 8(a), we can see that the measured FAD fluorescence initially rises a little and reaches the maximum at around 0.7 mm before decreasing to around 0.1 at a focal depth of 5.5 mm with a sharp drop at focal depths between 0.7 and 2.7 mm. In Fig. 8(b), the measured PpIX fluorescence rises slightly from the zero focal depth, which reaches the maximum at 0.7 mm, and then decreases slowly to 0.24 at a focal depth of 5.5 mm. The trends in the Monte Carlo simulations are similar to the measured results. Figures 8(c) and 8(d) show the close match between experimental and simulated sensitivities to the top and bottom layers in the cone shell-cone shell configuration. The sensitivity to the top layer in the simulated result is around 0.53 at a zero focal depth, slightly higher than that in the experimental result which is 0.51. Both sensitivities drop as the focal depth increases. The simulated sensitivity value reaches its minimum of 0.30 at a focal depth of around 4.8 mm and the experimental sensitivity reaches its minimum of 2.9 at a focal depth of 5.5 mm. The sensitivities to the bottom layer in experimental and simulated results are 0.49 and 0.47 at a zero focal depth and increase to around 0.71 in the experiment and 0.7 in the simulations at a focal depth of 5.5 mm.

Figure 9 shows the comparison in the sensitivity to the top and bottom layers achieved by the four different illumination-detection configurations as illustrated in Fig. 1. In Fig. 9(a),

a decreasing trend in the sensitivity to the top layer in each configuration can be observed when the focal depth increases from 0 to 5.5 mm. Generally, when focusing at the surface of the phantom, axicon lens-based setups show higher sensitivities to the top layer than the convex lens-based setups. This may be related to the fact that the axicon lens forms a focal line instead of a focal spot which is the case of the convex lens. When one focuses the center part of the focal line formed by an axicon lens on the surface of the phantom, part of the focal line penetrates deeper into the phantom and excites more signal from the illuminated regions. Thus, FAD fluorescence is relatively more excited at a zero focal depth in an axicon setup, which elevated the sensitivity to the top layer. By comparing the sensitivities to the top layer achieved by the two cone shell-cone configurations implemented by different lenses, it can be seen that apart from the difference at small focal depths where the axicon lens-based setup shows superior sensitivity, the two setups have similar sensitivities to the top layer with a minimum sensitivity around 0.3 at a focal depth of 5.5 mm. In contrast, the cone-cone configuration achieved a minimum sensitivity to the top layer of 0.38 at a focal depth of 5.5 mm. The comparison clearly demonstrates that the cone shell illumination configuration can significantly reduce fluorescence contribution from the top layer when performing deep measurements. When a cone shell detection geometry is used in addition to a cone shell illumination configuration, as shown by the solid black line in Fig. 9(a), the minimum sensitivity to the top layer at a focal depth of 5.5 mm is further lowered by about 7% to 0.28%. This result suggests that the cone shell-cone shell configuration
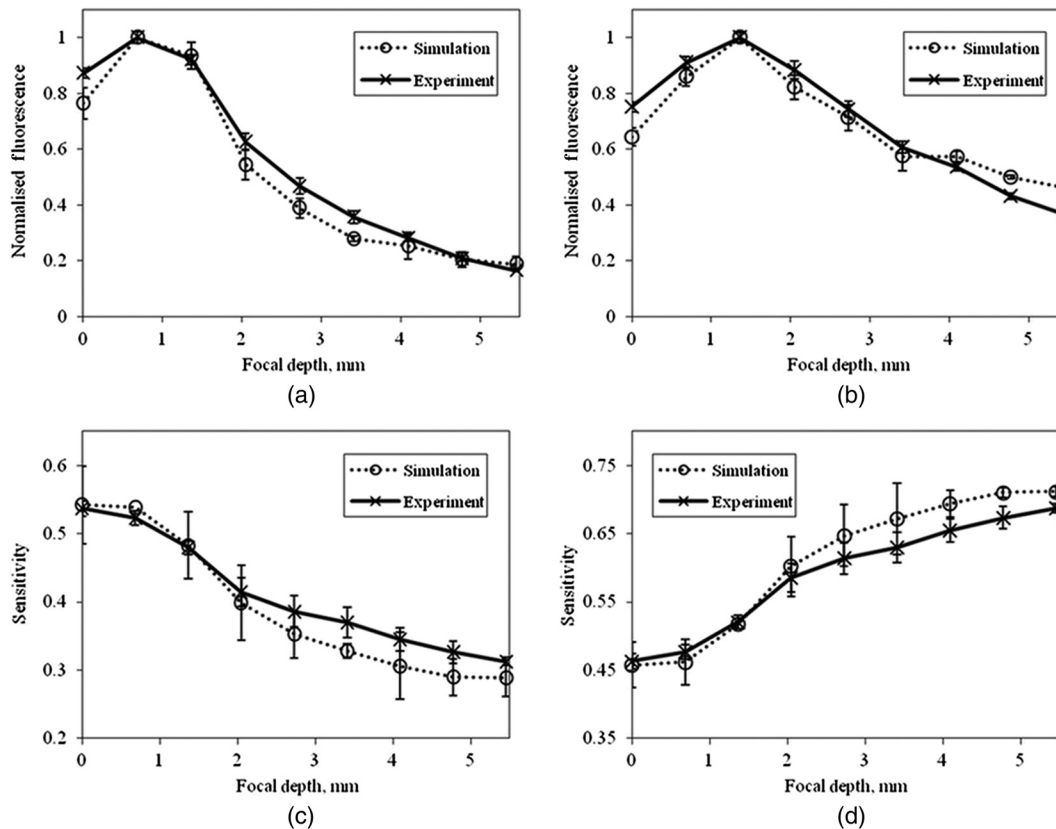
Fig. 7 (a) Normalized FAD fluorescence and (b) normalized PpIX measured from the tissue phantom using the cone shell-cone configuration as shown in Fig. 1(c), and the corresponding simulated results, (c) sensitivity to top layer and (d) sensitivity to bottom layer computed from the experimental and simulated results. Focal depth refers to the targeted depth of focus beneath the phantom surface, which has been corrected for the refractive mismatch between the phantom and air.

is most suitable for depth sensitive measurements in a turbid medium. When the cone shell illumination configuration reduces the contribution of fluorescence from shallower layers, the cone shell detection configuration rejects out-of-focus fluorescence from those nontargeted depths that would otherwise reach the probe.

Comparatively, in Fig. 9(b), one can see an increasing trend in the sensitivity to the bottom layer in each configuration when the focal depth increases from 0 to 5.5 mm. Due to more fluorescence collected from the top layer by the axicon lens-based setups at a zero focal depth as explained above, the sensitivity to the bottom layer of the two axicon setups is lower than that of the convex lens-based setups. At a focal depth of 5.5 mm, the cone shell-cone shell configuration has the highest sensitivity to the bottom layer of 0.72, followed by both the cone shell-cone configuration with a sensitivity of around 0.7 and the cone-cone configuration with a sensitivity of 0.62.

It is noted that the two cone shell-cone configurations implemented by the axicon and the convex lenses, respectively, as represented by the gray and dashed lines in Figs. 9(a) and 9(b), demonstrate similar sensitivities to the top and bottom layers at all focal depths except at the zero focal depth where the axicon lens-based setup shows better sensitivities. However, the axicon lens-based setup has its own disadvantages. For example, an axicon lens is usually weaker than the convex lens setup in terms of the focusing and signal collection power due to the intrinsic structure. For fluorescence measurements from the

superficial region of a tissue model, the axicon lens-based setups would require a considerably higher laser power and acquisition time than the convex lens-based setups to achieve a similar signal-to-noise ratio. Moreover, the formation of an elongated focal line by the axicon lens can affect the axial resolution of the measurements compared to those achieved by a convex lens where a more confined laser focus can be formed. However, the axial resolution of axicon lens-based setups can be improved by minimizing the length of the focal line formed by using a thinner excitation ring (smaller d as shown in Fig. 3). Theoretically, the excitation ring thickness, d, is half of the incident laser beam diameter, D, as shown in Fig. 3. A pair of axicon lens with identical apex angles, Axicons 1 and 2, can steer the angle of the excitation beam, splitting it into a collimated annular ring with a thickness equal to half of the original beam diameter. Unfortunately, a portion of the excitation beam can pass through (instead of being refracted) the center of the axicon lens in its original direction and illuminates the sample in our experiment due to the imperfection at the axicon lens's tip. Therefore, in the experiments performed for this study, a relatively larger excitation laser beam diameter of 3 mm was used to minimize the influence of light passing through the center of the axicon lens on the measured results. Consequently, a longer laser focal line was formed that reduces the axial resolution and focusing power of the axicon lens-based setups. The imperfect tips of the axicon lenses could be one of the reasons for the slight deviation between the experimental and simulated results as shown in Figs. 7 and 8.
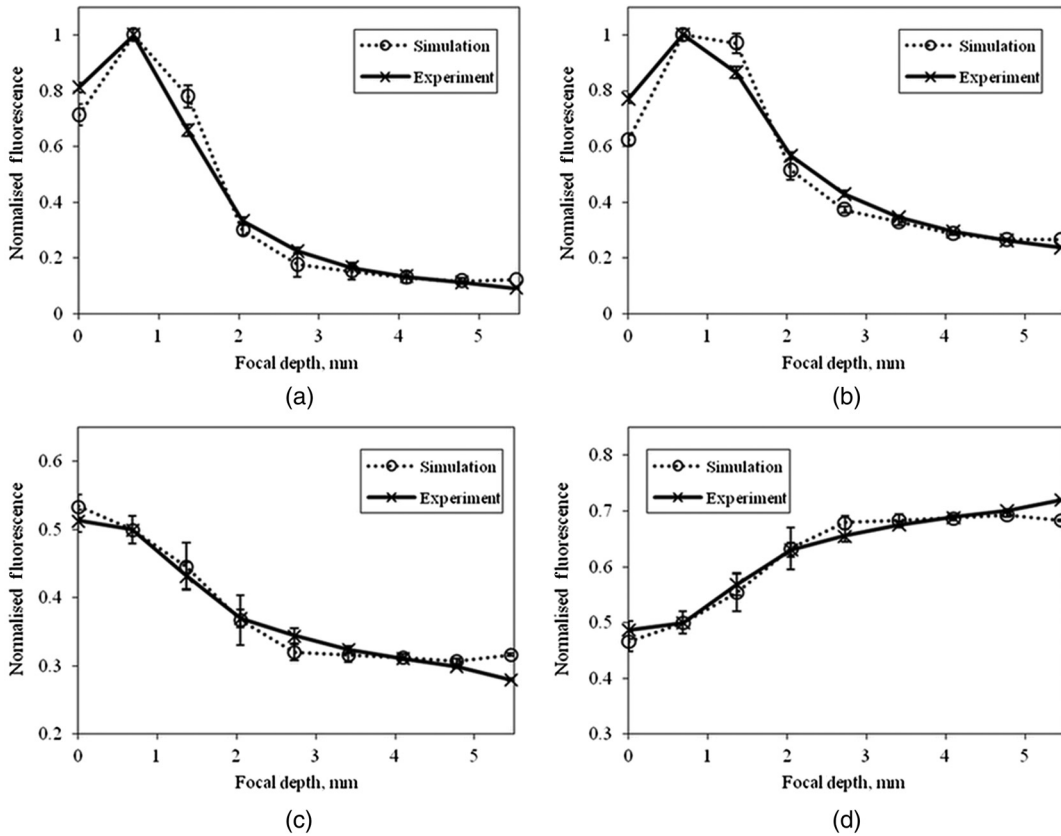
Fig. 8 (a) Normalized FAD fluorescence and (b) normalized PpIX fluorescence measured from the tissue phantom using the cone shell-cone shell configuration as shown in Fig. 1(d), and the corresponding Monte Carlo simulation results, (c) sensitivity to the top layer and (d) sensitivity to the bottom layer computed from the experimental and simulated results. Focal depth refers to the targeted depth of focus beneath the phantom surface, which has been corrected for the refractive mismatch between the phantom and air.

Although the convex lenses are superior to the axicons in terms of the power of light focusing and signal collection, they require that the lens–sample distance be altered in order to measure from different depths in a sample. In many clinical applications, such as skin cancer screening, a device without the need for precisely tuning the distance to the target is preferable as it offers the physician flexibility to measure from various parts of the body and can save the time used for fine tuning. The difficulties in varying the device-sample distance accurately and maintaining that distance throughout measurements have limited the use of convex lens-based setups for depth sensitive measurements in such clinical applications. Axicon lens-based setups for depth sensitive measurements without the need to move any component(s) up and down will bring a significant
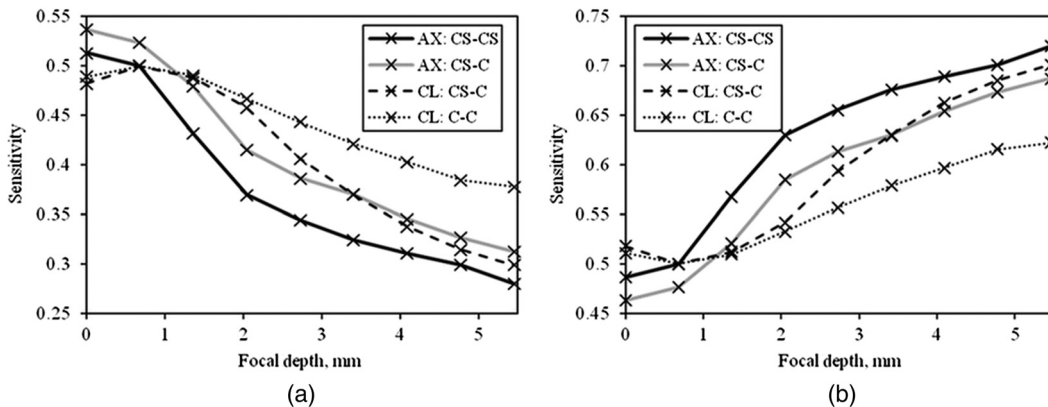

Fig. 9 Comparison in the sensitivity to the (a) top layer and (b) bottom layer achieved by the four different optical configurations in the epithelial tissue phantom. AX refers to axicon lens; CL refers to convex lens; CS refers to the cone shell configuration and C refers to the cone configuration. The focal depth refers to the targeted depth of focus beneath the phantom surface, which has been corrected for the refractive mismatch between the phantom and air.

convenience to these clinical applications, which could reduce the measurement uncertainty induced by the inconsistency in the device-sample distance compared to the convex lens-based setups.

Another issue is the potential influence of the coherence property on light propagation in our experiments. Although laser light was used to excite the fluorescence in our experiments, light coherence was not accounted for in the Monte Carlo modeling of this study for the following reasons. The 405-nm laser source, which was used in the free space mode in our experiment, has a line width of 1–2 nm and a coherence length of smaller than 5 mm. The optical path length from the laser source to the sample in our experimental setup was around 50 cm, which was much larger than the coherence length of the laser light. The degree of coherence of the laser light that reached the top surface of the axicon lens has dramatically dropped and the coherence effect of the light in the sample can be negligible in this case. Therefore, the modeling of such minimally coherent light, if not totally incoherent, through the axicon lens or propagation in the sample did not require the consideration of coherence phenomena such as diffraction. The validity of this approach has been proven by the good agreement between the experimental and simulation results.

7 Conclusion

In this study, we have investigated the depth sensitivity of four illumination and detection configurations involving the conventional cone and novel cone shell geometry implemented by a convex lens or an axicon lens in a turbid medium. The results show that a cone shell illumination configuration was able to reduce the fluorescence contribution from the overlaying layers when performing deep measurements as compared to a cone illumination configuration. A cone shell detection configuration can reject undesired fluorescence from off-focus regions, hence giving the best depth sensitivity in conjunction with a cone shell illumination configuration. The use of convex or axicon lenses in implementing the illumination-detection configurations has no profound effect on the depth sensitivity. However, both the lenses are suitable for different clinical applications due to their own pros and cons and none of them is superior over the other. To facilitate the optimization of the optical system, we have developed a Monte Carlo simulation to model the convex and axicon lenses in implementing the cone and cone shell illumination and detection configurations. The simulation results were validated against the experimental results in terms of fluorescence intensity and depth sensitivity. This Monte Carlo code will be a useful tool that helps in planning and optimization of optical designs involving cone or cone shell configurations and axicon or convex lenses prior to the real experimental study.

We would like to highlight that the Monte Carlo codes for simulating fluorescence propagation in a fiber-optic probe geometry and a convex lens-based geometry will be made publically available.[26]

References

1. R. Richards-Kortum and E. Sevick-Muraca, "Quantitative optical spectroscopy for tissue diagnosis," *Ann. Rev. Phys. Chem.* **47**(1), 555–606, (1996).
2. N. Ramanujam, "Fluorescence spectroscopy of neoplastic and non-neoplastic tissues," *Neoplasia* **2**(1–2), 89–117 (2000).
3. G. A. Wagnieres, W. M. Star, and B. C. Wilson, "In vivo fluorescence spectroscopy and imaging for oncological applications," *Photochem. Photobiol.* **68**(5), 603–632 (1998).
4. M. Follen et al., "Effects of biographical variables on cervical fluorescence emission spectra," *J. Biomed. Opt.* **8**(3), 479–483 (2003).
5. E. M. Gill et al., "Relationship between collagen autofluorescence of the human cervix and menopausal status," *Photochem. Photobiol.* **77**(6), 653–658 (2003).
6. R. Drezek et al., "Autofluorescence microscopy of fresh cervical-tissue sections reveals alterations in tissue biochemistry with dysplasia," *Photochem. Photobiol.* **73**(6), 636–641 (2001).
7. I. Pavlova et al., "Microanatomical and biochemical origins of normal and precancerous cervical autofluorescence using laser-scanning fluorescence confocal microscopy," *Photochem. Photobiol.* **77**(5), 550–555 (2003).
8. T. J. Pfefer et al., "Selective detection of fluorophore layers in turbid media: the role of fiber-optic probe design," *Opt. Lett.* **28**(2), 120–122 (2003).
9. L. Quan and N. Ramanujam, "Relationship between depth of a target in a turbid medium and fluorescence measured by a variable-aperture method," *Opt. Lett.* **27**(2), 104–106 (2002).
10. Q. Liu and N. Ramanujam, "Experimental proof of the feasibility of using an angled fiber-optic probe for depth-sensitive fluorescence spectroscopy of turbid media," *Opt. Lett.* **29**(17), 2034–2036 (2004).
11. L. Lim et al., "Probe pressure effects on human skin diffuse reflectance and fluorescence spectroscopy measurements," *J. Biomed. Opt.* **16**(1), 011012 (2011).
12. S. F. Bish et al., "Development of a noncontact diffuse optical spectroscopy probe for measuring tissue optical properties," *J. Biomed. Opt.* **16**(12), 120505 (2011).
13. M. Mazurenka et al., "Non-contact time-resolved diffuse reflectance imaging at null source-detector separation," *Opt. Express* **20**(1), 283–290 (2012).
14. Y. H. Ong and Q. Liu, "Axicon lens-based cone shell configuration for depth-sensitive fluorescence measurements in turbid media," *Opt. Lett.* **38**(15), 2647–2649 (2013).
15. M. Keijzer et al., "Fluorescence spectroscopy of turbid media: autofluorescence of the human aorta," *Appl. Opt.* **28**(20), 4286–4292 (1989).
16. L. H. Wang, S. L. Jacques, and L. Q. Zheng, "MCML: Monte-Carlo modeling of light transport in multilayered tissues," *Comput. Meth. Prog. Bio.* **47**(2), 131–146 (1995).
17. L. H. Wang and S. L. Jacques, "Optimized radial and angular positions in Monte-Carlo modeling," *Med. Phys.* **21**(7), 1081–1083 (1994).
18. A. J. Welch et al., "Propagation of fluorescent light," *Lasers Surg. Med.* **21**(2), 166–178 (1997).
19. J. N. Qu et al., "Laser-induced fluorescence spectroscopy at endoscopy–tissue optics, Monte Carlo modeling, and in-vivo measurements," *Opt. Eng.* **34**(11), 3334–3343 (1995).
20. C. F. Zhu, Q. Liu, and N. Ramanujam, "Effect of fiber optic probe geometry on depth-resolved fluorescence measurements from epithelial tissues: a Monte Carlo simulation," *J. Biomed. Opt.* **8**(2), 237–247 (2003).
21. C. Zhu and Q. Liu, "Numerical investigation of lens based setup for depth sensitive diffuse reflectance measurements in an epithelial cancer model," *Opt. Express* **20**(28), 29807–29822 (2012).
22. B. W. Pogue and G. Burke, "Fiber-optic bundle design for quantitative fluorescence measurement from tissue," *Appl. Opt.* **37**(31), 7429–7436 (1998).
23. Q. Liu, C. F. Zhu, and N. Ramanujam, "Experimental validation of Monte Carlo modeling of fluorescence in tissues in the UV-visible spectrum," *J. Biomed. Opt.* **8**(2), 223–236 (2003).
24. R. Cubeddu et al., "A solid tissue phantom for photon migration studies," *Phys. Med. Biol.* **42**(10), 1971–1979 (1997).
25. D. Arifler et al., "Spatially resolved reflectance spectroscopy for diagnosis of cervical precancer: Monte Carlo modeling and comparison to clinical measurements," *J. Biomed. Opt.* **11**(6), 064027 (2006).
26. Q. Liu et al., "Monte Carlo code for simulation of fluorescence from layered tissues," http://www.ntu.edu.sg/home/quanliu/ (16 July 2014).

Yi Hong Ong graduated with a BEng degree in biomedical engineering from the University of Malaya, Malaysia. He is currently a PhD student in the School of Chemical and Biomedical Engineering at Nanyang Technological University in Singapore. His current research is on the development of depth-sensitive optical measurement methods for medical diagnosis. He is interested in optical instrument development for medical imaging.

Caigang Zhu received his bachelor degree from Huazhong University of Science and Technology, and now he is a final year PhD candidate in the school of chemical and biomedical engineering at Nanyang

Technological University in Singapore. His main research interests include Monte Carlo modeling of light transport in tissue, optical spectroscopy, and imaging for cancer diagnosis.

Quan Liu received his BS degree in electrical engineering from Xidian University, Xi'an, China, his MS degree in electrical engineering from the Graduate School in Beijing, University of Science and Technology of China, and his PhD degree in biomedical engineering from the University of Wisconsin, Madison. He is currently an assistant professor in the School of Chemical and Biomedical Engineering at Nanyang Technological University (NTU) in Singapore.